processes

MDPI

Article

Nanoscale Pore Evolution of Terrestrial Shale with Thermal Maturation Level Increase Induced by Hydrous Pyrolysis

Haiyan Hu [1,2,3,*], Wangpeng Li [1,2], Yifan Yang [3] and Shuai Chen [3]

[1] State Key Laboratory of Shale Oil and Gas Enrichment Mechanisms and Efficient Development, Beijing 102206, China; liwp.syky@sinopec.com
[2] Sinopec Key Laboratory of Shale Oil/Gas Exploration and Production Technology, Beijing 102206, China
[3] School of Resource and Environment, Yangtze University, Wuhan 430100, China; yangyf2402@163.com (Y.Y.); chenshuai06162000@163.com (S.C.)
* Correspondence: hyhucom@163.com

Abstract: A series of terrestrial shale samples with different thermal maturities were subjected to hydrous artificial pyrolysis to study the evolution of terrestrial shale pores. The original shale was obtained from the terrestrial interval of a core sample, the total organic carbon (TOC) content was 8.34 wt%, and the vitrinite reflectance (R_o) was 5.31%. The original shale core was cut into eight parts, which were heated at temperatures of 300, 350, 400, 420, 450, 500, 550, and 600 °C to obtain samples with different thermal maturities. The pore size distribution (PSD), pore volume (PV), specific surface area (SSA), and pore types were investigated via CO_2 and N_2 adsorption tests and field emission scanning electron microscopy (FE-SEM). Many organic matter (OM) pores and mineral pores were observed via FE-SEM with increasing thermal maturity. The total PV and SSA increased until the sample reached 500 °C and then decreased, and the mesopore volume followed this trend. The micropore volume first decreased, increased until the sample reached 500 °C, and then decreased; the macropore volume increased to a peak in the sample pyrolyzed at 420 °C and then remained stable. Pores with sizes ranging from 10 to 30 nm were the predominant contributors to the shale pore volume. The SSA was affected by pores with diameters less than 20 nm, which accounted for approximately 54% of the SSA. The rate of OM conversion influenced pore creation.

Keywords: terrestrial shale; pore evolution; hydrous pyrolysis; gas adsorption measurement; FE-SEM

check for updates

Academic Editor: Fabrizio Scala

Received: 6 December 2024
Revised: 30 December 2024
Accepted: 11 January 2025
Published: 16 January 2025

Citation: Hu, H.; Li, W.; Yang, Y.; Chen, S. Nanoscale Pore Evolution of Terrestrial Shale with Thermal Maturation Level Increase Induced by Hydrous Pyrolysis. *Processes* **2025**, *13*, 246. https://doi.org/10.3390/pr13010246

Copyright: © 2025 by the authors. Licensee MDPI, Basel, Switzerland. This article is an open access article distributed under the terms and conditions of the Creative Commons Attribution (CC BY) license (https://creativecommons.org/licenses/by/4.0/).

1. Introduction

Shale gas exploration in marine intervals has been successful in recent decades in the U.S., China, Canada, etc., and many studies have focused on gas-bearing shales [1–9]. Shale pores are important for gas storage and resource evaluation and have gained much research attention [10–25]. Shale pores at various scales have been investigated via field emission scanning electron microscopy (FE-SEM), gas adsorption probes, such as CO_2, N_2, Ar, nuclear magnetic resonance (NMR), and nano-computed tomography (CT). The results of previous studies have revealed that organic matter pores are dominant in marine shales [3–16]. Shale pores are affected by the sedimentary environment, rock type, organic matter (OM) type, mineral composition, thermal maturity, etc. [2–16].

In China, shales deposited in terrestrial lacustrine environments are widely distributed, and terrestrial shale gas/oil has high resource potential and promising prospects for exploration and exploitation [4,20–39]. The Daanzhai Member lacustrine shale in the

Yuanba area, Sichuan Basin, had a high yield of approximately 200,000 m^3 per day during the gas test. Compared with those in marine shales, the pores in continental shales are different and more complicated, and the mineral pores and cracks in terrestrial shales are much more abundant [20–35].

Pore networks change with increasing thermal maturity during burial and diagenesis. The thermal maturity level is a key factor influencing shale pore evolution [6,12,14–22,27,40,41]. To investigate how temperature affects pores, some researchers have studied pore evolution in different mature geological shale samples or shale samples in which thermal states have been artificially induced via pyrolysis model experiments [42–47]. However, most investigations have focused on marine shales, and the original heated shale samples have been typically obtained from outcrops. Pore evolution in terrestrial shale has rarely been reported.

In this study, we focus on the pore network evolution of terrestrial shale and obtain various maturity samples by heating low-maturity terrestrial shale samples from cores. The main goals are to (1) study the pore type and morphology in the different mature shales via FE-SEM, (2) study the evolution of the pore size distribution (PSD) of micropores via CO_2 adsorption tests, and (3) study the evolution of the PSD of mesopores and macropores via N_2 sorption measurements.

2. Samples and Methods

2.1. The Original Shale Formation and Samples

A low-maturity terrestrial shale sample was selected from the Jurassic continental interval in a core from well C1, which is located in the northern Qaidam Basin in Northwest China, and the core sample was not highly affected by weathering and oxidation processes. The burial depth of the core was from 1921.25 m to 1978.35 m, which is the Jurassic interval, and the core length was 57.10 m. This interval of the core was deposited in an interactive sedimentary environment. The total organic carbon (TOC) contents of the Jurassic core shale from well C1 varied from 1.16 to 11.98%, with an average value of 4.16%. In total, the shale interval had a low thermal maturity, and the average vitrinite reflectance (R_o) was 0.51%. The oil shale appeared at burial depths ranging from 1920.50 m to 1929.71 m, had high TOC values, and contained some oil, and water could not permeate when dropped onto the core. A piece of black shale from the core was selected from this oil shale interval for the pyrolysis experiment.

2.2. Pyrolysis Simulation Experiment

This experiment was carried out with a high-temperature and high-pressure simulation instrument at the State Key Laboratory of Shale Oil and Gas of the Wuxi Branch Institute of Sinopec. The instrument was composed of heating, reaction, pressure control, and product receiver sections. This instrument was made for pyrolysis simulation experiments for many samples from sedimentary basins in China, such as the Bohai Bay Basin, Sichuan Basin, and Songliao Basin, and showed high stability and good reproducibility. Pyrolysis experiments of shale and mudstone have been induced about five hundred times since 2007, and this instrument was awarded the China National Technology Invention Second Prize in 2016 and was determined as the industry standard of China petroleum pyrolysis simulation in 2020. The opening and closing of the pressure valve were determined by the pressure difference being as high as 5 MPa. To obtain a series of different mature samples, the core was divided into eight pieces, and the experimental conditions are listed in detail in Table 1.

Table 1. Hydrous pyrolysis experiment data of the continental shale samples.

Reaction Temperature	Raised Rate	Reaction Time	Simulation Depth	Lithostatic Pressure	Hydrodynamic Pressure
(°C)	(°C/min)	(h)	(m)	(MPa)	(MPa)
300	1	48	2500	49	25
350	1	48	3700	89	37
400	1	48	5000	125	50
420	1	48	5500	138	55
450	1	48	5900	148	59
500	1	48	6100	153	61
550	1	48	7100	176	71
600	1	48	7900	196	79

Eight shale samples were cut vertically to the bedding planes of the shale. Every sample weighed about 20–30 g and was loaded into eight sample cells, respectively. These eight sample cells were cleaned completely before the loaded samples to prevent contamination and ensure consistency across experiments. The burial depths in the simulation were similar to those of the Wufeng–Longmaxi Formations and Daanzhai Member in the Sichuan Basin. The overlying rock pressure and hydrostatic pressure in the intervals were set on the basis of the combined burial history of the Longmaxi shale and Daanzhai Member (Table 1). The experiments began after a leak test and evacuation were completed. Pyrolysis was performed under isothermal conditions at temperatures of 300 °C, 350 °C, 400 °C, 420 °C, 450 °C, 500 °C, 550 °C, and 600 °C for 48 h, and the heating rate was 1 °C per minute. Once the experiments were finished, all the products were collected in the product system. The yielded gas was collected in the pre-evaluated gas holder via the displacement of saturated brine. The total gas capacity was measured via the ideal gas equation. The liquid product was the sum of expelled oil from the shale. The pyrolysis shale samples with various thermal levels were divided into two parts: one was used for the FE-SEM observations and vitrinite reflectance measurements and the other was powdered to approximately 100 mesh for the TOC, rock evaluation, and CO_2 and N_2 adsorption tests.

2.3. TOC, Vitrinite Reflectance (R_o), and XRD Analyses

The TOC content was determined via a CS-200 sulfur-carbon detector produced by the American Leica Company. The analysis involved grinding the sample to a size of 0.15 mm, removing the inorganic carbon with dilute hydrochloric acid, drying it, and then burning the treated sample in an oxygen flow at a high temperature (1200 °C) to convert the organic carbon into CO_2, which was then determined by an infrared detector.

OM was converted to oil and gas during thermal maturity; we defined the converted OM ratio as calculated via Equation (1) [40] as follows:

$$C_i = (TOC_o - TOC_i)/TOC_o \times 100\% \quad (1)$$

where C_i is the converted OM ratio; TOC_o represents the TOC value of the original shale sample, which was used for the pyrolysis experiment; and TOC_i represents the TOC value of the ith pyrolysis temperature of the shale sample.

The vitrinite reflectance (R_o) of each sample was examined via an MPV-SP spectrophotometer produced by the German Leica Company. At room temperature, at least 20 vitrinite reflectance measurements were taken for each sample. The reflectance R_o was examined under oil immersion by the use of a 50×/0.85 objective lens.

Semi-quantitative mineral composition measurements were made on the samples by the use of X-ray diffraction (XRD); the instrument was a Bruker D8 Advance X-ray

diffractometer, and the work condition was under 30 mA and 40 kV. Stepped scanning measurements were made at a speed of 4°/min at a width of 3–85° (2θ); the relative contents of the mineral were determined under the area of the major peak curve of each mineral with correction for Lorentz Polarization.

2.4. Gas Adsorption Measurements and FE-SEM

For the CO_2 and N_2 gas adsorption tests, an Autosorb-iQ-MP instrument was used to measure the specific surface area (SSA) and PSD of each shale sample. The samples were powered to 60–80 mesh in size, and 2–4 g of sample was measured in the absorption tests after drying and degassing. The shale samples were automatically outgassed at a temperature of approximately 110 °C and were under vacuum for approximately 12 h to eliminate volatile matter and moisture before measurement, regardless of N_2 or CO_2. Liquid nitrogen with a purity greater than 99.999% was used in the adsorption probe. The PSD, PV, and SSA were obtained on the basis of theoretical models. CO_2 adsorption experiments can characterize micropores (<2 nm in diameter) because the diameter of the CO_2 molecule is only 0.33 nm, and the parameters of PSD, PV, and SSA can be obtained via different theoretical models. The model assumption is that the total isotherm consists of the number of individual single-pore isotherms multiplied by their relative distribution over a range of pore sizes.

The eight shale samples were polished with a Leica triple mill to observe the pores in the shales via Zeiss Merlin FE-SEM without any coating, which can provide photographs of many pores less than 10 nm in diameter. The observation limit measured by FE-SEM is a 2 nm pore diameter. A combination of a secondary electron and a backscattered electron mode was used. The working distance of the Zeiss Merlin FE-SEM instrument ranged from approximately 4 to 6 mm. The working accelerating voltage varied from 1 to 1.5 kV to prevent damage to the milled smooth surface by the electronic beam.

We chose an area of 5000×; mineral pores and OM pores were both obtained within the area of the 5000× image. The OM pores were captured as follows. First, OM grains were selected randomly, and photographs of whole OM grains were taken; second, OM pore photographs of approximately 50,000× were randomly collected within the OM pellets. When possible, artifact pores were eliminated during sample preparation. Mineral pores were imaged with a relatively low-speed lens at approximately 10,000× to 30,000×.

3. Results and Discussion

3.1. Geochemical Parameters and Pyrolysis Yields

The original shale TOC was 8.34% and the hydrogen index (HI) was 836.4 mg/g TOC, indicating type I kerogen in the shale (Table 2). The TOC contents of the eight pyrolysis shale samples ranged from 3.72 to 8.24%, with an average of 5.68%. The Rock-Eval S_1 values ranged from 0.47 to 7.87 mg/g, with an average of 2.11 mg/g. S_2 values ranged from 0.10 to 69.77 mg/g, with a mean of 18.70 mg/g. HI values ranged from 2.69 to 836.37 mg/g TOC, with a mean value of 243.83 mg/g TOC. This original shale was buried at a depth of 1926.58 m, the TOC content was 8.34 wt%, the vitrinite reflectance (R_o) was 5.31%, the Rock-Eval T_{max} was 432 °C, the S_1 value was 7.87 mg/g, the S_2 value was 69.77 mg/g, and the HI was 836.4 mg/g TOC (Table 2). The original shale composition consisted of quartz, 38.5%, feldspar, 5.5%, calcite, 0.2%, dolomite, 0.8%, siderite, 3.3%, and clay mineral, 50.8%.

The oil yield values ranged from 3.64 to 207.16 mg/g TOC, with a mean value of 120.28 mg/g TOC, during the pyrolysis simulation. The hydrocarbon gas yield values ranged from 2.08 to 304.55 cm^3/g TOC, with an average value of 167.35 cm^3/g TOC.

Table 2. The shale sample geochemistry parameters and yields.

Sample ID	TOC (wt %)	Hydrocarbon Gas (cm^3/g TOC)	Oil (mg/g TOC)	S_1 (mg/g)	S_2 (mg/g)	T_{max} (°C)	HI (mg/g TOC)	R_o (%)
C1-1926.58	8.34			7.87	69.77	449	836.4	0.53
300	8.24	2.08	3.64	1.60	62.51	439	758.6	0.54
350	6.71	13.36	190.45	3.61	27.75	439	413.6	0.72
400	4.30	95.98	207.16	2.24	6.04	441	140.5	1.02
420	4.95	144.72	177.59	1.00	1.12	572	22.6	1.30
450	5.03	262.28	120.08	0.89	0.45		8.9	1.95
500	5.30	294.27	82.56	0.75	0.44		8.3	2.82
550	4.56	221.53	85.15	0.59	0.13		2.9	3.28
600	3.72	304.55	95.66	0.47	0.10		2.7	3.91

3.2. Pore Types

The original lacustrine shale contained mainly pores between minerals and intrapores within the clay minerals (Figure 1a). Mineral pores became much more abundant than those in marine shales with increasing thermal maturity, which was different from the situation in marine shales [6–19]. When the pyrolysis temperature was greater than 400 °C, the mineral pores were numerous and very large compared with those in the 300 °C and 350 °C samples (Figure 2a–h). At 400 °C, many dissolution pores in the calcite formed, indicating that organic acid was produced and created solution pores (Figure 1c–e) [6,17,19,40]. Moreover, many types of mineral pores, such as large and long pores encircled by mineral particles or within mineral grains (Figure 1f–h) and short and thin cracks (Figure 1a–h), formed with increasing thermal maturity. The dense and short cracks were associated with illite mineral formation, and the large pores encircled in the mineral rims possibly resulted from the combination of gas-generation expansion and dissolution caused by organic acid, which occurred in the Longmaxi shale, the Marcellus, and the Barnett shales [6,14,17,19].

The OM contained few pores, such as those between the OM and mineral interface and the primary pores inside the OM particles (Figure 2a). Overall, the OM had almost no pores, indicating that many OM pores probably need to be created in the process of converting kerogen to oil and gas (Figure 2a–h). The samples heated to temperatures of less than 400 °C revealed that the OM pores were primary pores in the OM, and some pores were probably produced during the process of converting OM to kerogen. Large and round bubble-like OM pores appeared in the sample that was pyrolyzed at 450 °C (Figure 2e), possibly indicating the beginning of gas generation and the presence of pores associated with oil drops and gas escape [6,12,17,19,40]. At the same time, spongy OM pores were observed in the samples with temperatures greater than 400 °C (Figure 2d–h), and some shrinkage OM pores and microfractures were discovered in the samples, possibly due to hydrocarbon expulsion [17,19,40].

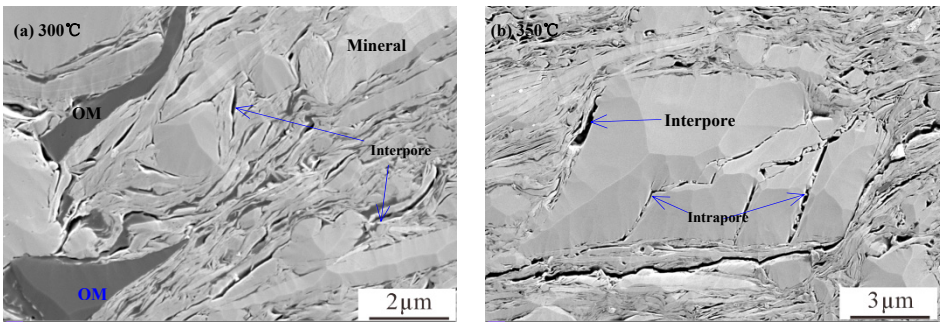

Figure 1. *Cont.*

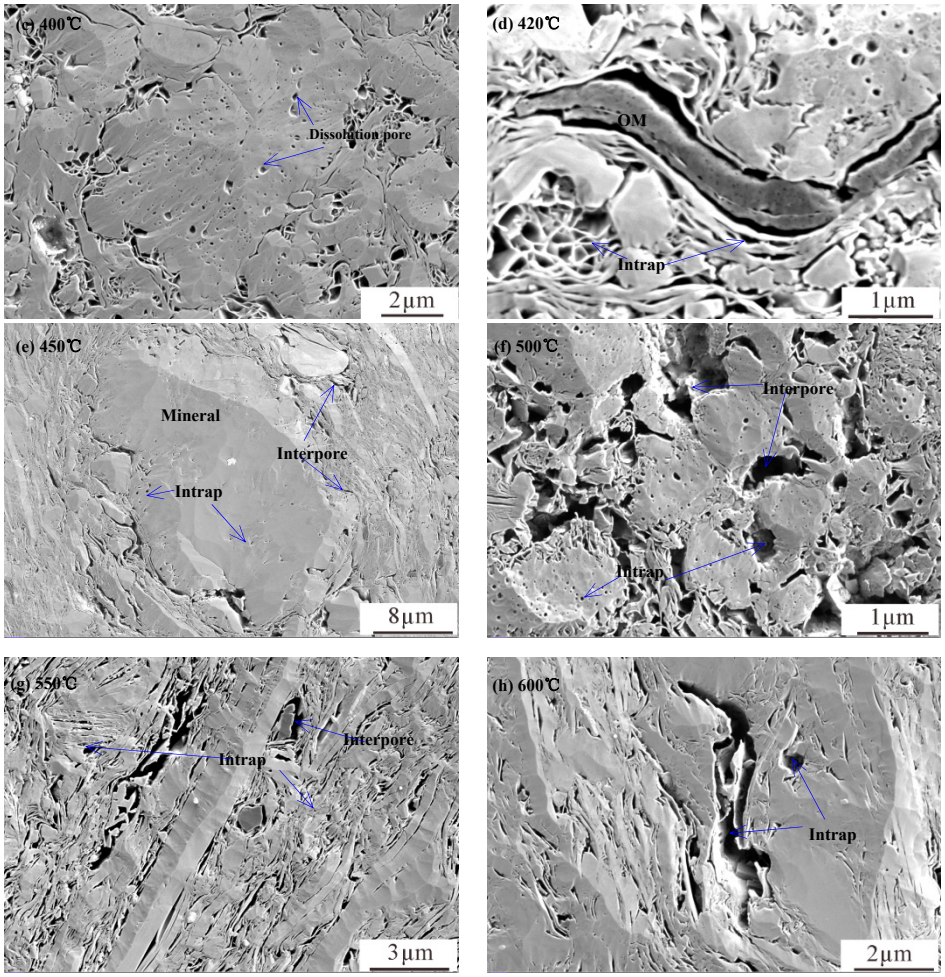

Figure 1. Mineral pore (blue arrows pointing) images in the pyrolysis samples under FE-SEM.

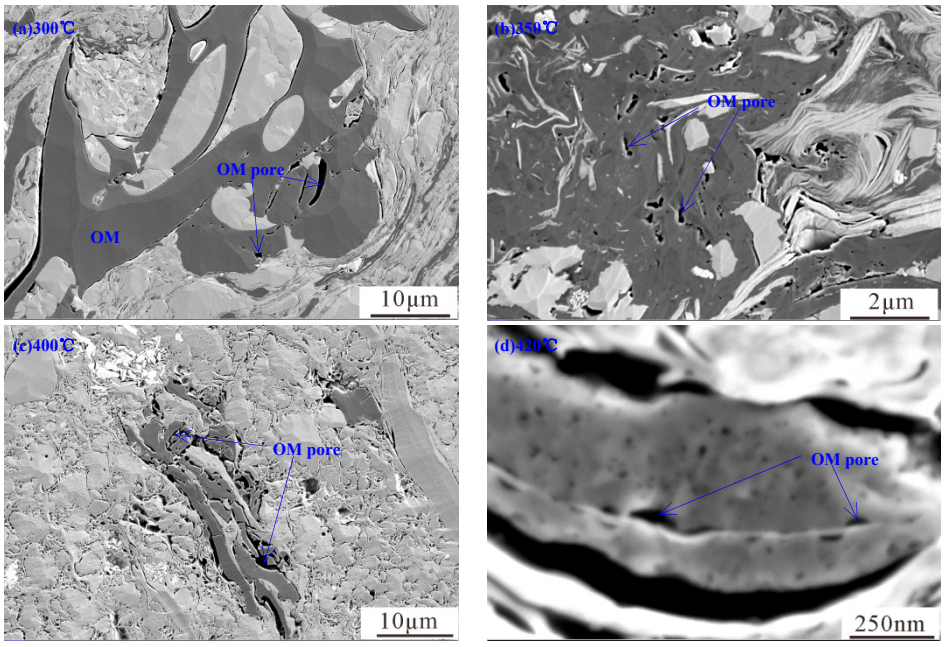

Figure 2. *Cont.*

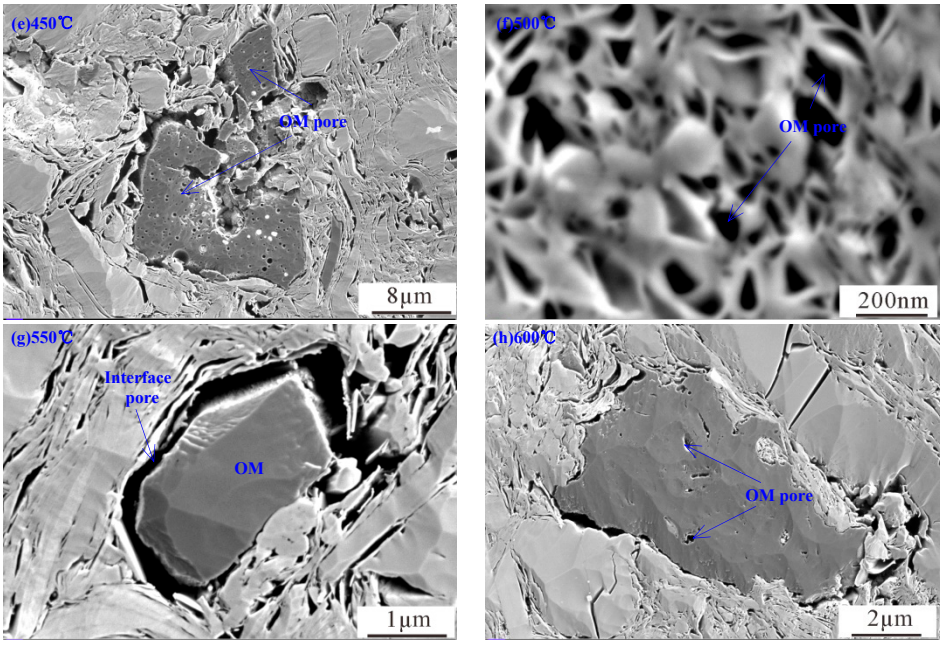

Figure 2. OM pore (blue arrows pointing) images in the pyrolysis samples under FE-SEM.

Compared with the marine shales, such as Wufeng–Longmaxi shale, which was predominantly an OM pore [6,15,20,41], these artificial thermal samples have abundant mineral pores and minor OM pores, which was consistent with the observation results of continental shale Daanzhai Member [24,27], suggesting that these samples can represent the continental shale pore evolution to some extent.

3.3. Micropores and SSA Determined by the CO_2 Adsorption Test

The CO_2 adsorption capacity increased with increasing pyrolysis temperature and ranged from 0.11 to 0.34 cm^3/g. The CO_2 adsorption capacity of the sample at 350 °C was the lowest, at 0.11 cm^3/g, and that of the sample at 500 °C was the highest, at 0.34 cm^3/g (Figure 3a, Table 3). The sample with the lowest micropore volume, 0.22 mm^3/g, was produced at a pyrolysis temperature of 350 °C, and the sample with the greatest micropore volume, 0.82 mm^3/g, was produced at a pyrolysis temperature of 500 °C (Figure 3b, Table 3). The pore volume rapidly increased between 0.5 and 0.9 nm in diameter for all samples; however, the samples pyrolyzed at 500 °C had more pores with diameters greater than 0.9 nm, and the cumulative pore volume still increased rapidly when the pore diameter was greater than 0.9 nm (Figure 3b). Overall, the shale pore volume increased with increasing thermal level, peaked at 500 °C, and then decreased. OM pores and mineral pores both clearly increased with increasing thermal maturity (Figures 1a–h and 2a–h). OM pores typically have a relatively small pore diameter according to marine shale observations [6,12,17,19,40], and as a result, we infer that the micropores predominantly consist of OM pores. The SSAs ranged from 0.55 to 1.97 m^2/g on the basis of the CO_2 sorption data (Tables 3 and 4), which was much lower than the SSA of marine shale micropores, and the micropore SSA in marine shale typically accounts for 60% of the total shale SSA [6,15,20,41].

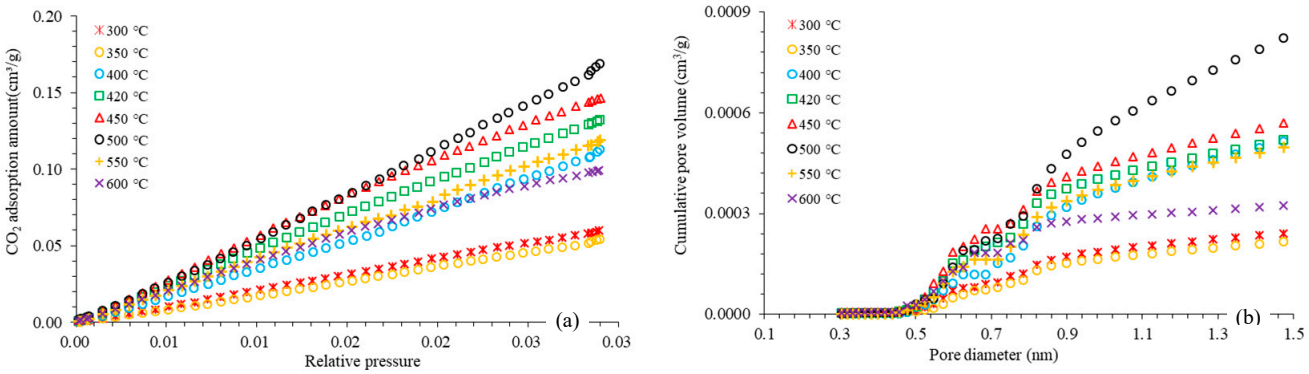

Figure 3. CO_2 adsorption amount (**a**) and the cumulative pore volume (**b**) of the samples with thermal maturity induced by pyrolysis.

Table 3. Different pore size volumes of the pyrolysis shale samples.

Sample ID	Pore Volume (mm^3/g)										
	<10 nm	10–20 nm	20–30 nm	30–40 nm	40–50 nm	50–60 nm	60–70 nm	70–80 nm	Micropore	Mesopore	Macropore
300	1.00	3.00	3.00	2.00	3.00	2.00	2.00	1.00	0.24	11.59	5.48
350	0.22	3.00	5.00	4.00	5.00	4.00	4.00	2.00	0.22	19.14	11.00
400	4.00	12.00	11.00	8.00	8.00	6.00	6.00	4.00	0.51	41.60	16.59
420	3.33	14.00	13.00	10.00	11.00	8.00	8.00	4.00	0.52	50.70	19.67
450	6.70	13.00	12.00	8.00	9.00	7.00	7.00	5.00	0.57	48.85	18.09
500	4.62	15.00	14.00	10.00	11.00	8.00	8.00	5.00	0.82	54.11	20.81
550	4.70	12.00	12.00	9.00	10.00	7.00	8.00	5.00	0.50	47.76	20.86
600	2.02	14.00	13.00	9.00	9.00	7.00	8.00	5.00	0.32	47.77	20.43

Table 4. Different pore size volume ratios of the pyrolysis shale samples.

Sample ID	Pore Volume Ratio (%)										
	<10 nm	10–20 nm	20–30 nm	30–40 nm	40–50 nm	50–60 nm	60–70 nm	70–80 nm	Micropore	Mesopore	Macropore
300	5.9	17.6	17.6	11.8	17.6	11.8	11.8	5.9	1.4	67.0	31.6
350	0.8	11.0	18.4	14.7	18.4	14.7	14.7	7.3	0.7	63.0	36.2
400	6.8	20.3	18.6	13.6	13.6	10.2	10.2	6.8	0.9	70.9	28.3
420	4.7	19.6	18.2	14.0	15.4	11.2	11.2	5.6	0.7	71.5	27.7
450	9.9	19.2	17.7	11.8	13.3	10.3	10.3	7.4	0.8	72.4	26.8
500	6.1	19.8	18.5	13.2	14.5	10.6	10.6	6.6	1.1	71.4	27.5
550	6.9	17.7	17.7	13.3	14.8	10.3	11.8	7.4	0.7	69.1	30.2
600	3.0	20.9	19.4	13.4	13.4	10.4	11.9	7.5	0.5	69.7	29.8

3.4. N_2 Adsorption Experimental Data, Mesopores, and Macropores

The sample N_2 experimental isotherms consisted of adsorption and desorption lines, which did not completely coincide and exhibited a hysteresis loop. The figure shows the type H3 hysteresis loop based on the N_2 curves with increasing thermal maturity (Figure 4a,b), indicating that the pores were mainly open slits and conical holes and that these pores had good connectivity, which was consistent with the FE-SEM observations (Figures 1a–h and 2a–h). The N_2 sorption capacities ranged from 202.97 to 819.22 cm^3/g, and the mean was 625.98 cm^3/g; the lowest value was from the sample with a pyrolysis temperature of 300 °C, and the highest value was from the sample with a pyrolysis temperature of 450 °C (Figure 4a,b).

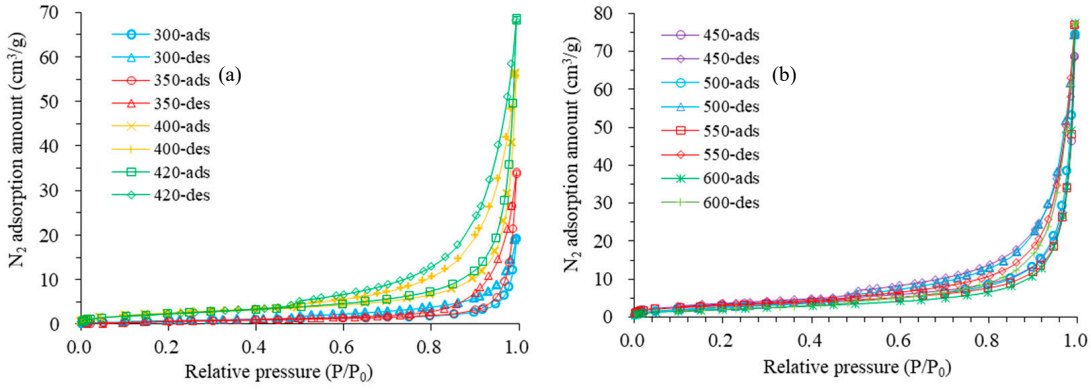

Figure 4. N_2 adsorption amount with the increasing thermal maturity induced by pyrolysis: (**a**) the samples from 300 to 420 °C; (**b**) the samples from 450 to 600 °C.

The cumulative pore volumes varied from 17.07 to 56.69 mm^3/g, with an average of 56.69 mm^3/g, according to the DTF model based on N_2 adsorption experimental data (Figure 5a, Table 3). The PSD data revealed that multiple peaks existed in the samples; however, there were some variations between the samples. The samples at pyrolysis temperatures of 300 and 350 °C lacked peaks ranging from 10 to 15 nm (Figure 5b, Tables 3 and 4), suggesting that the small pores need to reach relatively high thermal maturity levels, and at thermal maturities greater than 400 °C, the PSD had four peaks and greater pore volume, suggesting that many pores were created during the conversion of OM to oil and gas, which was confirmed by the FE-SEM images (Figures 1a–h and 2a–h).

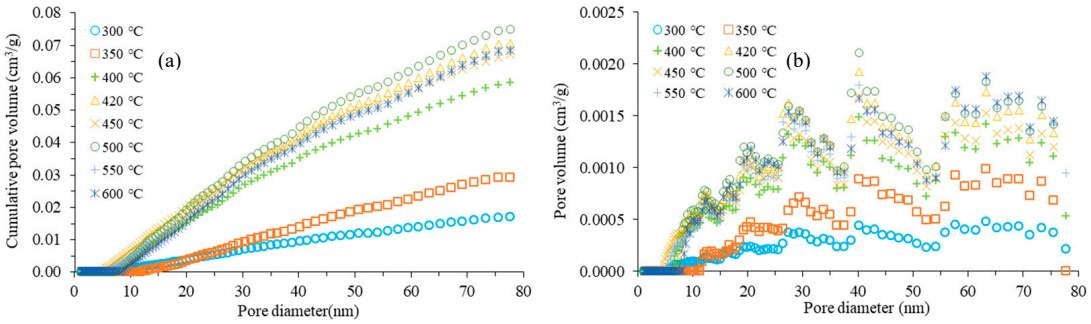

Figure 5. Cumulative pore volume (**a**) and PSD (**b**) based on N_2 adsorption data.

The SSAs changed from 2.57 to 11.91 m^2/g, with a mean of 8.79 m^2/g. The SSAs of the mesopores varied from 2.22 to 10.76 m^2/g, with a mean of 7.74 m^2/g; the SSAs of the macropores ranged from 0.35 to 1.33 m^2/g, with a mean of 1.05 m^2/g (Tables 5 and 6).

Table 5. Different pore-specific surface areas of the pyrolysis shale samples.

Sample ID	Specific Surface Area (m^2/g)										
	<10 nm	10–20 nm	20–30 nm	30–40 nm	40–50 nm	50–60 nm	60–70 nm	70–80 nm	Micropore	Mesopore	Macropore
300	1.10	0.78	0.46	0.27	0.27	0.14	0.13	0.07	0.62	2.22	0.35
350	0.55	0.96	0.84	0.51	0.51	0.29	0.26	0.12	0.55	2.77	0.64
400	2.88	3.20	1.69	0.93	0.93	0.45	0.39	0.21	1.25	8.20	1.06
420	2.64	3.95	2.13	1.15	1.15	0.55	0.48	0.23	1.37	9.46	1.26
450	4.87	3.69	1.89	0.98	0.98	0.49	0.42	0.24	1.52	10.76	1.15
500	3.73	4.27	2.18	1.18	1.18	0.57	0.51	0.25	1.97	10.42	1.33
550	3.45	3.42	1.96	1.05	1.05	0.54	0.50	0.28	1.28	9.51	1.32
600	1.68	3.74	2.12	1.10	1.10	0.53	0.52	0.25	0.94	8.61	1.30

Table 6. Different pore-specific surface area ratios of the pyrolysis shale samples.

Sample ID	Specific Surface Area Percentage (%)										
	<10 nm	**10–20 nm**	**20–30 nm**	**30–40 nm**	**40–50 nm**	**50–60 nm**	**60–70 nm**	**70–80 nm**	**Micropore**	**Mesopore**	**Macropore**
300	34.0	24.1	14.3	8.5	8.5	4.4	4.1	2.3	19.5	69.7	10.9
350	13.6	23.6	20.8	12.7	12.7	7.2	6.4	3.1	14.0	69.9	16.1
400	26.9	29.9	15.8	8.7	8.7	4.2	3.7	2.0	11.9	78.0	10.1
420	21.5	32.2	17.3	9.4	9.4	4.5	3.9	1.9	11.4	78.2	10.4
450	35.9	27.2	13.9	7.2	7.2	3.6	3.1	1.8	11.3	80.1	8.6
500	26.9	30.8	15.7	8.5	8.5	4.1	3.6	1.8	14.4	75.9	9.7
550	28.1	27.9	16.0	8.6	8.6	4.4	4.1	2.3	10.6	78.5	10.9
600	15.2	33.9	19.2	10.0	10.0	4.8	4.7	2.3	8.7	79.3	12.0

3.5. Pore Evolution Influenced by Thermal Maturity

Both CO_2 and N_2 adsorption capacity rose with the increasing pyrolyzed temperatures, which were the index of thermal maturity; therefore, maturity clearly affects pore development in continental shale, which is consistent with that of marine shale [6,12,17,19,40].

The nanopore can be divided into the micropore (<2 nm), mesopore (2–50 nm), and macropore (>50 nm) based on the pore diameter [48]. The total pore volume and SSA increased with increasing temperature (Figure 6a,b); however, micropores and mesopores were predominant in the sample pyrolyzed at 500 °C and then gradually decreased; macropores increased to a peak in the sample pyrolyzed at 420 °C and then changed little (Figure 6a, Table 3). The macropores may have been mainly mineral pores and remained stable after consolidation diagenesis. For the clay minerals, pores were possibly created during the process of converting smectite to illite [6,40]; at the same time, the intervals were already sufficient and protected the pores from damage by compaction. Micropores decreased sharply in the sample heated at 350 °C, and the ratio of micropores decreased from 1.4% to 0.7% (Figure 6c, Tables 3 and 4), possibly because the pores were filled by generated bitumen and oil, while mesopores and macropores were produced. The mesopore and macropore volumes increased in the sample pyrolyzed at 350 °C; however, the mesopore volume ratio decreased, and the macropore volume ratio increased, which was puzzling and needs to be investigated in the future, and we inferred that this phenomenon was associated with acid dissolution. After the sample was heated at 500 °C, the micropore and mesopore volumes and their percentages decreased, probably because the pores damaged by cementation were more numerous than the pores created by hydrocarbon generation and illite conversion. Overall, the mesopore percentage increased with increasing thermal maturity; however, the macropore percentage decreased with increasing thermal maturity (Figure 6c, Tables 3 and 4), probably because many mesopores were produced, and macropores resulted from compaction and cementation. The artificial samples revealed the micropore accounted for 0.8%, the mesopore for 69.4%, and the macropore for 29.8%, and these pore volume ratios to some extent were according to the Chang 7 shale in the Ordos Basin [24,27], indicating that these samples can stand for the continental shale pore evolution trend. However, in the overmature marine shales, micropores consisted of about 28.2% of the total pore volume, mesopores consisted of about 66.4%, and macropores consisted of about 5.2% [6,15,20,41].

The SSA of micropores and macropores increased with increasing thermal maturity, peaked at a pyrolysis temperature of 500 °C, and then gradually decreased, and their percentages were similar. The mesopore SSA peaked at a pyrolysis temperature of 450 °C and exhibited the same trend as the total SSA of the shale samples. The mesopore SSA percentage accounted for an average of 69.4%, which was clearly different from the SSA of marine shale, which was predominantly attributed to micropores, the SSA of which

accounted for about 67.8% [6,15,20,41]. The distinction of the pore ratio and SSA between marine shale and continental shale needs to be further researched in the future.

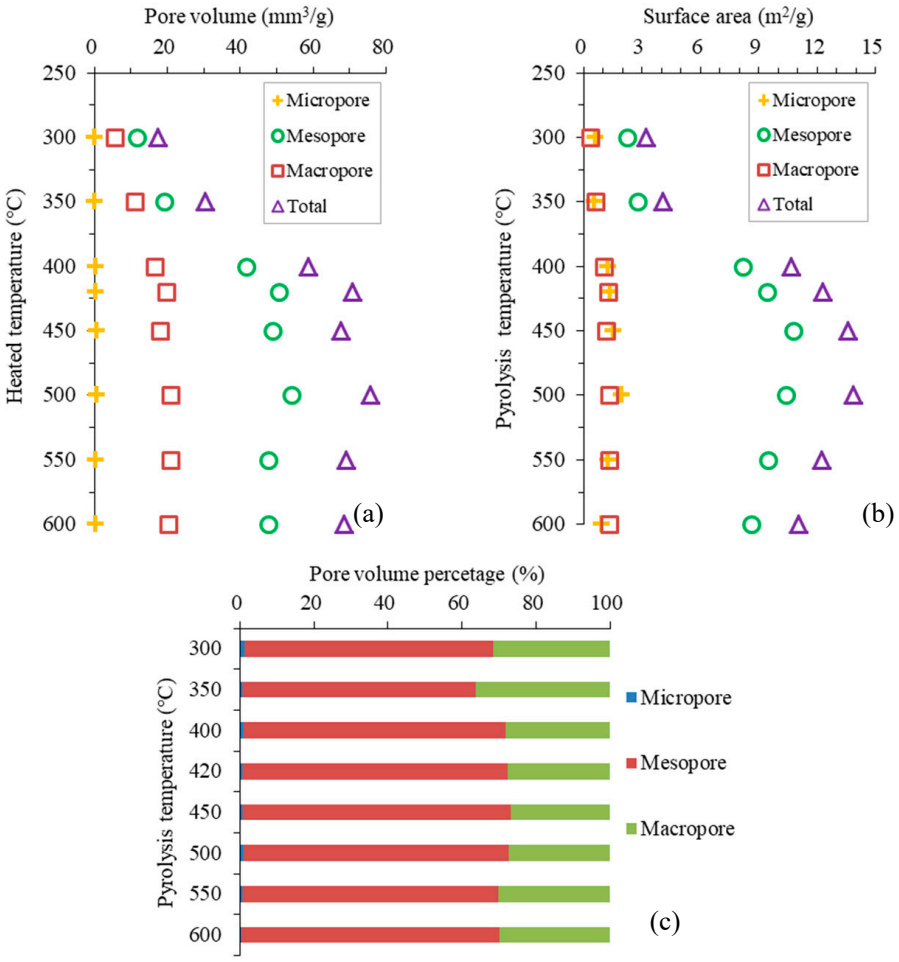

Figure 6. Pore volume and surface area evolution with increasing thermal maturity induced by pyrolysis. (**a**) Pore volume variation of micropores, mesopores, macropores, and total pores; (**b**) surface area; (**c**) pore volume ratios.

To determine different size pore relative contributions, these pores were divided into <10 nm, [10–20) nm, [20–30) nm, [30–40) nm, [40–50) nm, [50–60) nm, [60–70) nm, [70–80) nm pore size widths based on the diameter (Figure 7a,b, Table 3 and 4). Pores in diameter from 10 to 30 nm consisted of an average of 36.5% of all pore volume in the OM maturity progresses. The increasing amplitudes of pore volumes were pores with diameters of less than 20 nm, pores with sizes of less than 10 nm raised from 0.8 to 9.9%, and pores with diameters from 10 to 20 nm, enhanced from 11 to 20.9% (Figure 8a,b, Tables 3 and 4). Pores with diameters of less than 20 contributed to an average of 54% of the SSA, and pores <10 nm and 10–20 nm in diameter accounted for 25.3% and 28.7% of the SSA, respectively (Figure 8a,b Tables 5 and 6), and an SSA of less than a 20 nm wide pore had the highest increased amplitude. These were different from the marine shales, whose SSAs were composed of pores with diameters of less than 10 nm [6,15,20,41].

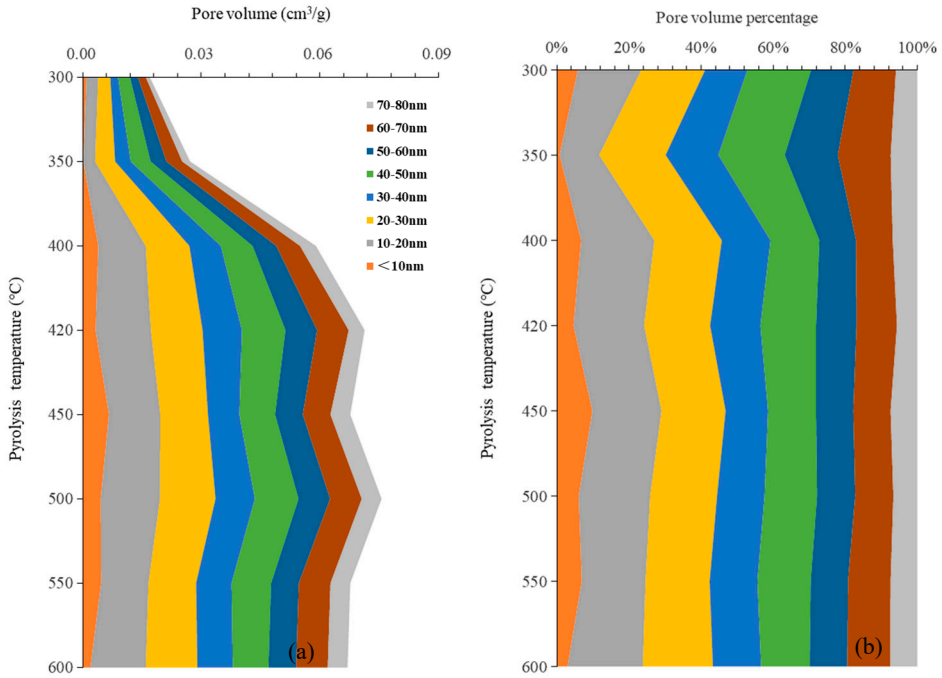

Figure 7. Volume of different pore sizes (**a**) and pore volume percentage (**b**) with thermal maturity.

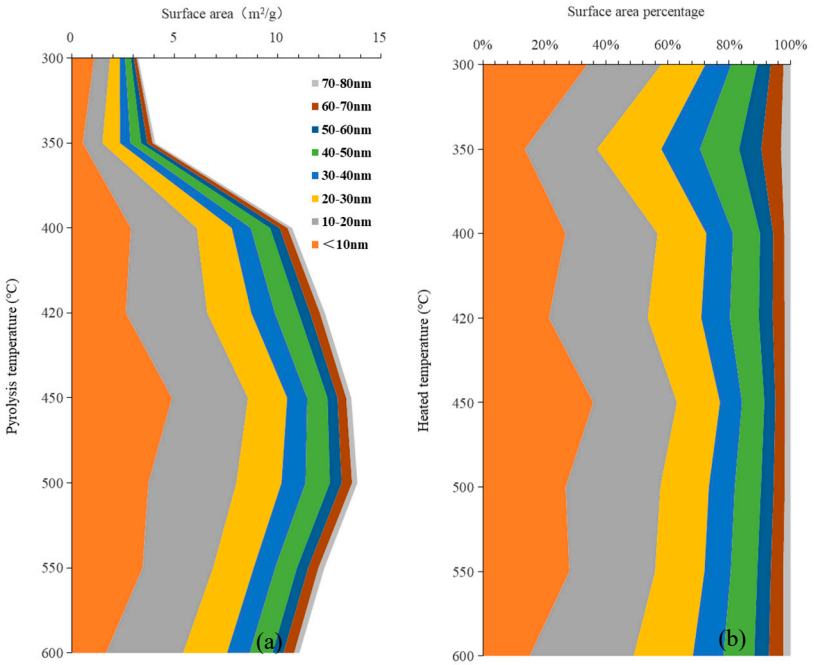

Figure 8. SSA of different pore sizes (**a**) and SSA percentage (**b**) with thermal maturity.

This pore evolution can give some indications. (1) The terrestrial oil shale in China has medium maturity and developed mineral pores and a good reservoir. (2) The high-maturity terrestrial gas shale, such as the Ziliujing Formation shale, has abundant pores and good reservoirs. (3) For the overmature mature shale, such as the Niutitang Formation, we can focus on the shales mixed with some terrestrial shale compositions. It should be noted that the pyrolysis simulation cannot completely stand for the geological evolution process, and we should understand the differences and limitations.

3.6. Impact of OM Conversion on Pore Development

As previously mentioned, both the pore volume and type increased sharply, indicating that OM conversion obviously affected pore evolution. Therefore, the converted OM rate was used to investigate pore evolution during hydrocarbon generation. The converted OM rate had an obvious correlation with the mesopore volume and macropore volume but instead had only a minor relationship with the micropore volume (Figure 9a); the SSA of micropores and mesopores was impacted by the OM conversion ratio and had little effect on macropores (Figure 9b). Typically, the micropore was associated with OM conversion based on the results of marine shales [6,15,41]; however, micropore volume had a weak relation with the OM conversion rate, and it had a strong correlation with the SSA of the micropore; the OM conversion rate affected the mesopore volume; however, it had a little relationship with the SSA of the mesopore. As observed under the SEM (Figures 1a–h and 2a–h), the terrestrial shale can create lots of mineral pores during thermal maturity, and these pores were large; therefore, the OM version rate revealed a strong relationship with mesopore volume and macropores. Although these pores were not produced within OM, they were associated with the OM version process. For the micropore, the possible cause was that the OM version yield occupied the pore and reduced the micropore volume; as a result, the micropore showed a weak correlation with the OM version rate. The product exists with some micropores, and these pores offer the SSA. The results of the micropore were puzzling, and they need to be further investigated in the future.

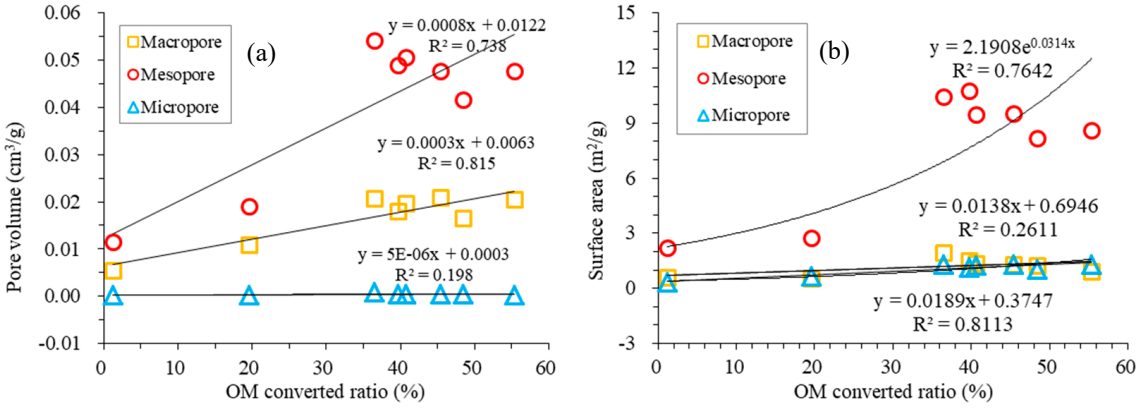

Figure 9. The correlation between the OM converted rate and pore volume and SSA. (**a**) The OM converted ratio and pore volume; (**b**) the OM converted rate and SSA.

4. Conclusions

The different maturity shale samples were induced by the artificial pyrolysis experiments, and their pores were researched by the use of FE-SEM, N_2, and CO_2 adsorption measurements. Some conclusions can be made as follows.

The different maturity stages of the shale samples were investigated via artificial pyrolysis experiments, and their pores were researched via FE-SEM and N_2 and CO_2 adsorption measurements. The conclusions are as follows:

1. Many OM pores and mineral pores can both be produced largely during the process of OM thermal maturity. Dissolution pores, slit clay pores, cracks, and fractures were observed with increasing thermal maturity. OM pores included round and large pores, spongy pores, and elongated interface pores located between the OM and minerals.
2. With increasing maturity levels, the evolution of pores exhibited a complicated trend: the total pore volume and SSA increased until peaking at 500 °C and then decreased. In addition, different sizes of pores displayed various patterns. The number of macropores peaked in the sample pyrolyzed at 420 °C and then remained stable;

the number of mesopores increased until the sample was pyrolyzed at 500 °C and then decreased; the number of micropores first decreased and then increased until it peaked in the sample pyrolyzed at 500 °C and then decreased.

3. Pores with diameters ranging from 10 to 30 nm made relatively important contributions to the pore volume during the OM conversion process. The SSA was affected by pores with diameters of less than 20 nm, accounting for an average of 54% of the SSA.
4. The converted OM rate strongly influenced the mesopore volume, macropore volume, and SSA of micropores and mesopores.

Author Contributions: Conceptualization, H.H. and Y.Y.; investigation, H.H., W.L. and S.C.; resources, W.L.; writing—original draft preparation, H.H.; writing—review and editing, H.H. and S.C.; supervision, H.H.; project administration, W.L.; funding acquisition, Y.Y. All authors have read and agreed to the published version of the manuscript.

Funding: This investigation was funded by the Open Fund Project of Sinopec Key Laboratory of Shale Oil/Gas Exploration and Production Technology (Contract No. 33550000-22-ZC0613-0219) and the NNSFC (Grant No. 41472122).

Data Availability Statement: The data presented in this study are openly available in [Shao Z] at [https://doi.org/10.1016/j.coal.2022.103936], reference number [39].

Acknowledgments: We thank the China Geological Survey Bureau for offering the original shale samples.

Conflicts of Interest: The authors declare no conflicts of interest.

References

1. Curtis, J.B. Fractured shale-gas systems. *AAPG Bull.* **2002**, *86*, 1921–1938.
2. Jarvie, D.M.; Hill, R.J.; Ruble, T.E.; Pollastro, R.M. Unconventional shale-gas systems: The Mississippian Barnett Shale of north-central Texas as one model for thermogenic shale-gas assessment. *AAPG Bull.* **2007**, *91*, 475–499. [CrossRef]
3. Hao, F.; Zou, H.Y. Cause of shale gas geochemical anomalies and mechanisms for gas enrichment and depletion in high-maturity shales. *Mar. Pet. Geol.* **2013**, *44*, 1–12. [CrossRef]
4. Hao, F.; Zou, H.Y.; Lu, Y.C. Mechanisms of shale gas storage: Implications for shale gas exploration in China. *AAPG Bull.* **2013**, *97*, 1325–1346. [CrossRef]
5. Hu, H.Y.; Hao, F.; Guo, X.S.; Dai, F.Y.; Lu, Y.C.; Ma, Y.Q. Investigation of methane sorption of overmature Wufeng-Longmaxi shale in the Jiaoshiba area, Eastern Sichuan Basin, China. *Mar. Pet. Geol.* **2018**, *91*, 251–261. [CrossRef]
6. Hu, H.Y.; Hao, F.; Lin, J.F.; Lu, Y.C.; Ma, Y.Q.; Li, Q. Organic matter-hosted pore system in the Wufeng-Longmaxi (O_3w-$S_1$1) shale, Jiaoshiba area, Eastern Sichuan Basin, China. *Int. J. Coal Geol.* **2017**, *173*, 40–50. [CrossRef]
7. Mishra, S.; Mendhe, V.A.; Varma, A.K.; Kamble, A.D.; Sharma, S.; Bannerjee, M.; Kalpana, M.S. Influence of organic and inorganic content on fractal dimensions of Barakar and Barren Measures shale gas reservoirs of Raniganj basin, India. *J. Nat. Gas Sci. Eng.* **2018**, *49*, 393–409. [CrossRef]
8. Sun, M.D.; Yu, B.S.; Hu, Q.H.; Zhang, Y.F.; Li, B.; Yang, R.; Melnichenko, Y.B.; Cheng, G. Pore structure characterization of organic-rich Niutitang shale from China: Small angle neutron scattering (SANS) study. *Int. J. Coal Geol.* **2018**, *186*, 115–125. [CrossRef]
9. Fishman, N.S.; Paul, C.; Hackley, P.C.; Lowers, H.; Hill, R.J.; Egenhoff, S.; Eberl, D.; Blum, A. The nature of porosity in organic-rich mudstones of the Upper Jurassic Kimmeridge Clay Formation, North Sea, offshore United Kingdom. *Int. J. Coal Geol.* **2012**, *103*, 32–50. [CrossRef]
10. Bernard, S.; Horsfield, B.; Schulz, H.M.; Wirth, R.; Schreiber, A.; Sherwood, N. Geochemical evolution of organic-rich shales with increasing maturity: A STXM and TEM study of the Posidonia Shale (Lower Toarcian, northern Germany). *Mar. Pet. Geol.* **2012**, *31*, 70–89. [CrossRef]
11. Bernard, S.; Wirth, R.; Schreiber, A.; Schulz, H.M.; Horsfield, B. Formation of nanoporous pyrobitumen residues during maturation of the Barnett Shale (FortWorth Basin). *Int. J. Coal Geol.* **2012**, *103*, 3–11. [CrossRef]
12. Löhr, S.C.; Baruch, E.T.; Hall, P.A.; Kennedy, M.J. Is organic pore development in gas shales influenced by the primary porosity and structure of thermally immature organic matter? *Org. Geochem.* **2015**, *87*, 119–132. [CrossRef]
13. Loucks, R.G.; Reed, R.M.; Ruppel, S.C.; Hammes, U. Spectrum of pore types and networks in mudrocks and a descriptive classification for matrix-related mudrock pores. *AAPG Bull.* **2012**, *96*, 1071–1098. [CrossRef]

14. Loucks, R.G.; Reed, R.M.; Ruppel, S.C.; Jarvie, D.M. Morphology genesis distribution of nanometer-scale pores in siliceous mudstones of the Mississippian Barnett Shale. *J. Sed. Res.* **2009**, *79*, 848–861. [CrossRef]
15. Mastalerz, M.; Schimmelmann, A.; Drobniak, A.; Chen, Y. Porosity of Devonian and Mississippian New Albany Shale across a maturation gradient: Insights from organic petrology, gas adsorption, and mercury intrusion. *AAPG Bull.* **2013**, *97*, 1621–1643. [CrossRef]
16. Milliken, K.L.; Esch, W.L.; Reed, R.M.; Zhang, T. Grain assemblages and strong diagenetic overprinting in siliceous mudrocks, Barnett Shale (Mississippian), Fort Worth Basin, Texas, U.S.A. *AAPG Bull.* **2012**, *96*, 1553–1578. [CrossRef]
17. Milliken, K.L.; Rudnicki, M.; Awwiller, N.D.; Zhang, T. Organic matter-hosted pore system, Marcellus Formation (Devonian), Pennsylvania. *AAPG Bull.* **2013**, *97*, 177–200. [CrossRef]
18. Modica, C.; Lapierre, S. Estimation of kerogen porosity in source rocks as a function of thermal transformation: Example from the Mowry Shale in the Powder River Basin of Wyoming. *AAPG Bull.* **2012**, *96*, 87–108. [CrossRef]
19. Pommer, M.; Milliken, K. Pore types and pore-size distributions across thermal manturity, Eagle ford Formation, southern Texas. *AAPG* **2015**, *99*, 1713–1744. [CrossRef]
20. Tian, H.; Pan, L.; Zhang, T.W.; Xiao, X.M.; Meng, Z.P.; Huang, B.J. Pore characterization of organic-rich Lower Cambrian shales in Qiannan Depression of Guizhou Province, Southwestern China. *Mar. Pet. Geol.* **2015**, *62*, 28–43. [CrossRef]
21. Zhang, Y.; Hu, Q.; Long, S.; Zhao, J.; Peng, N.; Wang, H.; Lin, X.; Sun, M. Mineral-controlled nm-μm-scale pore structure of saline lacustrine shale in Qianjiang Depression, Jianghan Basin, China. *Mar. Pet. Geol.* **2019**, *99*, 347–354. [CrossRef]
22. Zhu, D.; Jiang, Z.; Jiang, S.; Yang, W.; Song, Y.; Gao, Z.; Jiang, T.; Cao, X.; Li, W.; Zhang, Y. Water-bearing characteristics and their influences on the reservoir capacity in terrestrial shale reservoirs: A case study of the lower Jurassic Ziliujing Formation in the Northeast Sichuan Basin, China. *Mar. Pet. Geol.* **2021**, *123*, 104738. [CrossRef]
23. Zhang, W.; Xie, L.; Yang, W.; Qin, Y.; Peng, P. Micro fractures and pores in lacustrine shales of the Upper Triassic Yanchang Chang7 Member, Ordos Basin, China. *J. Pet. Sci. Eng.* **2017**, *156*, 194–201. [CrossRef]
24. Zhang, T.; Hu, S.; Bu, Q.; Bai, B.; Tao, S.; Chen, Y.; Pan, Z.; Lin, S.; Pang, Z.; Xu, W.; et al. Effects of lacustrine depositional sequences on organic matter enrichment in the Chang 7 Shale, Ordos Basin, China. *Mar. Pet. Geol.* **2021**, *124*, 104778. [CrossRef]
25. Xie, X.; Deng, H.; Fu, M.; Hu, L.; He, J. Evaluation of pore structure characteristics of four types of continental shales with the aid of low-pressure nitrogen adsorption and an improved FE-SEM technique in Ordos Basin, China. *J. Pet. Sci. Eng.* **2021**, *197*, 108018. [CrossRef]
26. Wu, T.; Zhao, J.; Zhang, W.; Zhang, D. Nanopore structure and nanomechanical properties of organic-rich terrestrial shale: An insight into technical issues for hydrocarbon production. *Nano Energy* **2020**, *69*, 104426. [CrossRef]
27. Wang, F.; Guo, S. Influential factors and model of shale pore evolution: A case study of a continental shale from the Ordos Basin. *Mar. Pet. Geol.* **2018**, *102*, 271–282. [CrossRef]
28. Teng, J.; Deng, H.; Liu, B.; Chen, W.; Fu, M.; Xia, Y.; Yu, H. Insights of the pore system of lacustrine shales from immature to late mature with the aid of petrology, mineralogy and porosimetry: A case study of the Triassic Yanchang Formation of the Ordos Basin, North China. *J. Pet. Sci. Eng.* **2021**, *196*, 107631. [CrossRef]
29. Tang, Y.; Yang, R.; Zhu, J.; Yin, S.; Fan, T.; Dong, L.; Hou, Y. Analysis of continental shale gas accumulation conditions in a rifted basin: A case study of Lower Cretaceous shale in the southern Songliao Basin, northeastern China. *Mar. Pet. Geol.* **2018**, *101*, 389–409. [CrossRef]
30. Zhang, H.; Zhu, Y.; Wang, Y.; Kang, W.; Chen, S. Comparison of organic matter occurrence and organic nanopore structure within marine and terrestrial shale. *J. Nat. Gas Sci. Eng.* **2016**, *32*, 356–363. [CrossRef]
31. Cao, Q.; Wen Zhou, W.; Deng, H.; Chen, W. Classification and controlling factors of organic pores in continental shale gas reservoirs based on laboratory experimental results. *J. Nat. Gas Sci. Eng.* **2015**, *27*, 1381–1388. [CrossRef]
32. Jiang, S.; Tang, X.; Cai, D.; Gang Xue, G.; Zhiliang He, Z.; Long, S.; Peng, Y.; Gao, B.; Xu, Z. Comparison of marine, transitional, and lacustrine shales: A case study from the Sichuan Basin in China. *J. Pet. Sci. Eng.* **2017**, *150*, 334–347. [CrossRef]
33. Wang, M.; Xie, W.; Huang, K.; Dai, X. Fine characterization of lithofacies and pore network structure of continental shale: Case study of the Shuinan Formation in the north Jiaolai Basin, China. *J. Pet. Sci. Eng.* **2019**, *175*, 948–960. [CrossRef]
34. Dai, J.; Zou, C.; Dong, D.; Ni, Y.; Wu, W.; Gong, D.; Wang, Y.; Huang, S.; Huang, J.; Fang, C.; et al. Geochemical characteristics of marine and terrestrial shale gas in China. *Mar. Pet. Geol.* **2016**, *76*, 444–463. [CrossRef]
35. Pan, S.; Zou, C.; Li, J.; Yang, Z.; Liu, E.; Han, Y. Unconventional shale systems: A comparative study of the "in-source sweet spot" developed in the lacustrine Chang 7 Shale and the marine Barnett Shale. *Mar. Pet. Geol.* **2019**, *100*, 540–550. [CrossRef]
36. Gao, F.; Song, Y.; Li, Z.; Xiong, F.; Chen, L.; Zhang, Y.; Liang, Z.; Zhang, X.; Chen, Z.; Joachim, M. Lithofacies and reservoir characteristics of the Lower Cretaceous continental Shahezi Shale in the Changling Fault Depression of Songliao Basin, NE China. *Mar. Pet. Geol.* **2018**, *98*, 401–421. [CrossRef]
37. Guo, H.; Jia, W.; He, R.; Yu, C.; Song, J.; Peng, P. Distinct evolution trends of nanometer-scale pores displayed by the pyrolysis of organic matter-rich lacustrine shales: Implications for the pore development mechanisms. *Mar. Pet. Geol.* **2020**, *121*, 104622. [CrossRef]

38. Han, H.; Pang, P.; Li, Z.-L.; Shi, P.-T.; Guo, C.; Liu, Y.; Chen, S.-J.; Lu, J.-G.; Gao, Y. Controls of organic and inorganic compositions on pore structure of lacustrine shales of Chang 7 member from Triassic Yanchang Formation in the Ordos Basin, China. *Mar. Pet. Geol.* **2018**, *100*, 270–284. [CrossRef]
39. Shao, D.; Zhang, T.; Zhang, L.; Li, Y.; Meng, K. Effects of pressure on gas generation and pore evolution in thermally matured calcareous mudrock: Insights from gold-tube pyrolysis of the Eagle Ford Shale using miniature core plugs. *Int. J. Coal Geol.* **2022**, *252*, 103936. [CrossRef]
40. Wang, Y.; Liu, L.; Hu, Q.; Hao, L.; Wang, X.; Sheng, Y. Nanoscale Pore Network Evolution of Xiamaling Marine Shale during Organic Matter Maturation by Hydrous Pyrolysis. *Energy Fuels* **2020**, *34*, 1548–1563. [CrossRef]
41. Hu, H.Y.; Zhang, T.W.; Wiggins-Camacho, J.D.; Ellis, G.S.; Lewan, M.D.; Zhang, X.L. Experimental investigation of changes in methane adsorption of bitumen-free Woodford Shale with thermal maturation induced by hydrous pyrolysis. *Mar. Pet. Geol.* **2015**, *59*, 114–128. [CrossRef]
42. Xiao, D.; Zheng, L.; Xing, J.; Wang, M.; Wang, R.; Guan, X.; Guo, X. Coupling control of organic and inorganic rock components on porosity and pore structure of lacustrine shale with medium maturity: A case study of the Qingshankou Formation in the southern Songliao Basin. *Mar. Pet. Geol.* **2024**, *164*, 106844. [CrossRef]
43. Fan, Q.; Cheng, P.; Gai, H.; Yu, Z.; Meng, G.; Xiao, X. Effects of post-oil bitumen on the nanopore development of shales: New insights from a stepwise thermal simulation experiment on small shale plug samples. *Mar. Pet. Geol.* **2024**, *168*, 107038. [CrossRef]
44. Wang, Y.; Yang, J. Origin of organic matter pore heterogeneity in oil mature Triassic Chang-7 mudstones, Ordos Basin, China. *Int. J. Coal Geol.* **2024**, *283*, 104458. [CrossRef]
45. Rao, Q.; He, Z.; Dong, T.; Wang, W.; Wang, X.; Rao, L.; Wang, T.; Huang, L. Pore and fracture characteristics and diagenetic evolution mechanisms of low-maturity lacustrine shales from the Paleogene Shahejie Formation in the Jiyang Depression, Bohai Bay Basin, Eastern China. *Mar. Pet. Geol.* **2024**, *170*, 107154. [CrossRef]
46. Liu, K.; Zhang, Z.; Safaei-Farouji, M.; Fattahi, E.; Zhang, H.; Liu, B.; Ostadhassan, M. Quantifying pore structure heterogeneity of shale samples after solvent extraction following anhydrous and hydrous pyrolysis. *Geoenergy Sci. Eng.* **2024**, *239*, 212978. [CrossRef]
47. Fatah, A.; Mahmud, H.; Bennour, Z.; Gholami, R.; Hossain, M. The impact of supercritical CO_2 on the pore structure and storage capacity of shales. *Nat. Gas Sci. Eng.* **2022**, *98*, 104394. [CrossRef]
48. IUPAC (International Union of Pure and Applied Chemistry). Physical chemistry division commission on colloid and surface chemistry, subcommittee on characterization of porous solids: Recommendations for the characterization of porous solids (technical report). *Pure Appl. Chem.* **1994**, *66*, 1739–1758. [CrossRef]

Disclaimer/Publisher's Note: The statements, opinions and data contained in all publications are solely those of the individual author(s) and contributor(s) and not of MDPI and/or the editor(s). MDPI and/or the editor(s) disclaim responsibility for any injury to people or property resulting from any ideas, methods, instructions or products referred to in the content.